Extreme Mechanics Letters 89 (2026) 102538

Contents lists available at ScienceDirect

Extreme Mechanics Letters

journal homepage: www.elsevier.com/locate/eml

Axisymmetric peeling of thin elastic films: Snap-through and wrinkling instabilities

Erteng Chen [a], Zheng Fang [b], Xianlong Wei [b,*], Zhaohe Dai [a,*]

[a] School of Mechanics and Engineering Science, State Key Laboratory for Turbulence and Complex Systems, Peking University, Beijing 100871, China
[b] Key Laboratory for the Physics and Chemistry of Nanodevices, School of Electronics, Peking University, Beijing 100871, China

ARTICLE INFO

Keywords:
Blister tests
Thin films
Snap through
Wrinkling
Peeling

ABSTRACT

Ultrathin elastic films are central to flexible electronics and sensing devices, where mechanical reliability is governed by the coupling between film elasticity and interfacial adhesion. Unlike bulk materials, these films are often characterized through out-of-plane loading into blister-like configurations. Although the mechanics of blisters at equilibrium have been extensively studied, the onset of blister formation remains less well understood, particularly because early-stage peeling can involve instability mechanisms such as snap-through and wrinkling. Here, we study the peeling of an ultrathin elastic film adhered to a rigid substrate under cylindrical loading, with van der Waals interactions incorporated at the interface. Using numerical simulations, scaling arguments, and linear stability analysis, we analyze the critical conditions for snap-through and the subsequent onset of wrinkling. We show that deformation outside the loading region contributes significantly to the critical peeling force, explaining the experimentally observed thickness dependence of the peak peeling force. We further determine the critical loading conditions and associated wrinkle modes, revealing how film elasticity and loading geometry govern wrinkle onset. The results enable the extraction of small-scale interfacial parameters that are difficult to obtain in steady-state blistering and also might be useful for applications that exploit these instability phenomena.

1. Introduction

Driven by the increasing demand for device miniaturization and integration [1], ultrathin films have become essential functional components in flexible electronics, sensors, and related technologies [2–4]. In many of these systems, robust film-substrate adhesion is required to maintain structural integrity and ensure reliable device operation [5–7]. Accurate characterization of interfacial properties such as adhesion energy is therefore critical [8]. However, as the film thickness decreases, conventional adhesion measurements, such as peel tests, become increasingly difficult to implement [9–12]. To address this challenge, blister tests [13,14] (which might be regarded as axisymmetric peel) have been developed and applied to thin films with thicknesses ranging from the subnanometer scale to microns [15–20].

Compared with one-dimensional peel, axisymmetric peel is governed by intrinsic geometric nonlinearities, making the evaluation of the energy release rate more subtle [21–23]. Recent theoretical advances have incorporated both geometric and constitutive nonlinearities, leading to tractable descriptions of the steady-state energy release rate in axisymmetric peel [24–28]. Beyond the steady state, however, a quantitative understanding of how the system approaches this state is also important for metrology and for applications involving film transfer and strain engineering [4,29,30]. For ultrathin films, resolving this early-stage peel process remains highly nontrivial [31–33]. Recent in situ experiments, for example, have shown that blister formation generally occurs only after the applied load reaches a critical value [19]. This abrupt transition is reminiscent of snap-through instabilities, which have also been observed during the formation of adhesive contact [34,35]. Moreover, in 2D material systems or liquid blister tests, this transition is often accompanied by wrinkling, which further alters the stress distribution and overall morphology of the film [15,36–38].

These observations motivate a quantitative study of the axisymmetric peel experiment, in which early-stage peel provides a direct route to probing instability-mediated interfacial mechanics in ultrathin films. Here, we examine how loading geometry, film thickness, and interfacial parameters govern the critical conditions for snap-through and wrinkling, and establish the corresponding scaling relations. The paper is organized as follows. Section 2 introduces the theoretical model and its nondimensionalization. Section 3 discusses the critical force for snap-through, analyzes its thickness dependence, and demonstrates

* Corresponding authors.
E-mail addresses: weixl@pku.edu.cn (X. Wei), daizh@pku.edu.cn (Z. Dai).

https://doi.org/10.1016/j.eml.2026.102538
Received 24 July 2026; Received in revised form 12 September 2026; Accepted 17 October 2026
Available online 28 October 2026
2352-4316/© 2026 Elsevier Ltd. All rights are reserved, including those for text and data mining, AI training, and similar technologies.

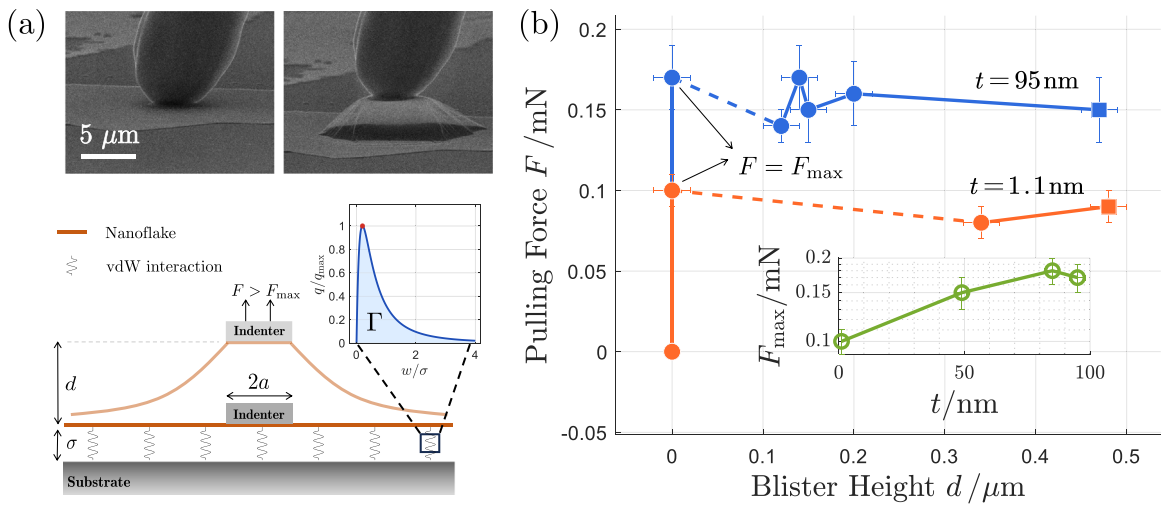


Fig. 1. (a) Scanning electron microscope (SEM) images of the axisymmetric peeling experiment of ∼1-nm-thick graphite flake, showing the occurrence of snap-through and wrinkling instabilities (upper panel); schematic illustration of the theoretical model (lower panel). The inset shows the normalized traction–separation relation for the van der Waals interaction described by Eq. (2.2). (b) Typical force–displacement curves measured in the axisymmetric peeling experiments on graphite nanoflakes [19]. The film undergoes snap-through (as indicated by the dashed line) after reaching the peak force F_{max}. The square marker at the end of the curve indicates rupture of the blister. The inset plots the experimentally measured critical force F_{max} as a function of film thickness t. The indenter radius is $a = 1.5$ μm for both datasets. Note that SEM images in this work are from tests on different samples following the method reported in [19], while the data in (b) are directly from [19].

how interfacial parameters can be extracted. Section 4 examines the onset of wrinkling, including the critical deflections and wrinkle modes. Finally, we summarize our main findings in Section 5.

2. A theoretical model

2.1. Governing equations

Inspired by the setup in Ref. [19] (see Fig. 1a), we consider the peeling of a nanoflake from a rigid substrate under cylindrical loading with radius a. Unlike previous studies showing delamination at the indenter-film interface [39], this type of debonding was not observed in repeated experiments reported in this work. The mechanical response of the flake is modeled as a continuum plate with thickness t, bending rigidity B, Poisson's ratio ν, and Young's modulus E. Since the focus is on the early stage of peeling, a normal van der Waals (vdW) traction is introduced over the entire film-substrate interface, thereby avoiding the need to track the delamination front explicitly [40,41]. Assuming linear elasticity and moderately large deflections, we employ the Föppl–von Kármán plate theory to describe the axisymmetric deformation of the nanoflake [42]. The emergence of wrinkles, which breaks this axisymmetric configuration [43], will be discussed in later sections.

Specifically, we denote the vertical deflection of the film (the upward displacement from its equilibrium position) as w, the out-of-plane equilibrium equation can then be written as:

$$B\nabla_r^2\left(\kappa_r+\kappa_\theta\right)-N_r\kappa_r-N_\theta\kappa_\theta+q(w)=F\frac{\delta(r-a)}{2\pi r}, \tag{2.1}$$

where $\nabla_r^2 f = \mathrm{d}^2 f/\mathrm{d}r^2 + r^{-1}\mathrm{d}f/\mathrm{d}r$ is the 2D axisymmetric Laplacian, $\delta(r)$ is the Dirac delta function. N_r and N_θ denote the radial and circumferential stress resultant, respectively. Also, $\kappa_r = \mathrm{d}^2 w/\mathrm{d}r^2$, $\kappa_\theta = r^{-1}\mathrm{d}w/\mathrm{d}r$ denote the radial and circumferential curvatures. The van der Waals traction $q(w)$ between the film and the substrate is described using the Lennard-Jones-type potential [41,44]:

$$q(w)=\frac{8\Gamma}{3\sigma}\left[\frac{1}{(w/\sigma+1)^3}-\frac{1}{(w/\sigma+1)^9}\right], \tag{2.2}$$

where Γ denotes the adhesion energy, and σ represents the equilibrium separation where $q = 0$. The resulting normalized traction–separation law is illustrated in the inset of Fig. 1a. In addition, the in-plane equilibrium equation must also be satisfied:

$$\frac{\mathrm{d}}{\mathrm{d}r}\left(rN_r\right)-N_\theta=0. \tag{2.3}$$

By introducing the Airy stress function φ with $N_r = r^{-1}\mathrm{d}\varphi/\mathrm{d}r$ and $N_\theta = \mathrm{d}^2\varphi/\mathrm{d}r^2$, in-plane equilibrium Eq. (2.3) is automatically satisfied and is replaced by the compatibility equation that the Airy stress function must satisfy:

$$r\frac{\mathrm{d}}{\mathrm{d}r}\left[\frac{1}{r}\frac{\mathrm{d}}{\mathrm{d}r}\left(r\frac{\mathrm{d}\varphi}{\mathrm{d}r}\right)\right]=-\frac{Et}{2}\left(\frac{\mathrm{d}w}{\mathrm{d}r}\right)^2. \tag{2.4}$$

Eqs. (2.1) and (2.4) define a complete boundary-value problem for φ and w, which requires seven boundary conditions. The far-field condition corresponds to the undisturbed state at infinity:

$$w,\frac{\mathrm{d}w}{\mathrm{d}r}\to 0 \quad\text{and}\quad \varphi\to\frac{1}{2}\gamma r^2 \quad\text{as}\quad r\to\infty, \tag{2.5}$$

where γ denotes the pre-tension in the film, which may arise from growth, transfer processes, or thermal mismatch [4,45,46]. At the edge of the loading region, a peeling height d and clamped boundary conditions are imposed:

$$w(a)=d,\quad w'(a)=0,\quad u(a)=\varphi''(a)-\nu\frac{\varphi'(a)}{a}=(1-\nu)\gamma,\quad \varphi(a)=0. \tag{2.6}$$

Finally, for a given d, the required peeling force F can be obtained by integrating the van der Waals traction over the entire interface. It is worth noting that, at later stages of delamination, the finite boundary of the film may influence the mechanics through effects such as interfacial sliding, which could invalidate the far-field boundary condition and even the axisymmetric assumption. However, for the early-stage peeling considered in this work, the far-field boundary condition is appropriate, as also confirmed numerically.

2.2. Nondimensionalization

Since the peeling process is governed by the van der Waals interaction at the film–substrate interface, its equilibrium separation σ provides a natural characteristic scale in the out-of-plane direction, while a lateral length

$$\ell_{\mathrm{vdW}}=\left(B\sigma^2/16\Gamma\right)^{1/4} \tag{2.7}$$

is introduced, representing the characteristic scale over which the bending strain energy density ($\sim B\sigma^2/\ell_{\rm vdW}^4$) is comparable to the adhesion energy per unit area (Γ). We then take the following nondimensionalization:

$$W=\frac{w}{\sigma},\ \delta=\frac{d}{\sigma},\ \eta=\frac{a}{\ell_{\rm vdW}},\ R=\frac{r}{\ell_{\rm vdW}},\ \Phi=\frac{\varphi}{B},\ \mathcal{F}=\frac{F}{4\sqrt{\Gamma B}},$$
$$\tau=\frac{\gamma\sigma}{4\sqrt{\Gamma B}},\ \mathcal{N}=\frac{N\sigma}{4\sqrt{\Gamma B}}. \tag{2.8}$$

Here, $\sqrt{\Gamma B}$ defines an elasto-adhesive force scale associated with lifting the film by a distance of order σ over the characteristic delamination scale $\ell_{\rm vdW}$ (balancing the external work $F\sigma$ with the adhesion energy $\Gamma\ell_{\rm vdW}^2$ gives $F\sim\sqrt{\Gamma B}$). With Eq. (2.8), we have the dimensionless forms of Eqs. (2.1) and (2.4):

$$\frac{1}{R}\frac{\mathrm{d}}{\mathrm{d}R}\left\{R\frac{\mathrm{d}}{\mathrm{d}R}\left[\frac{1}{R}\frac{\mathrm{d}}{\mathrm{d}R}\left(R\frac{\mathrm{d}W}{\mathrm{d}R}\right)\right]\right\}-\frac{1}{R}\frac{\mathrm{d}}{\mathrm{d}R}\left(\frac{\mathrm{d}\Phi}{\mathrm{d}R}\frac{\mathrm{d}W}{\mathrm{d}R}\right)+Q(W)=0 \tag{2.9}$$

and

$$R\frac{\mathrm{d}}{\mathrm{d}R}\left[\frac{1}{R}\frac{\mathrm{d}}{\mathrm{d}R}\left(R\frac{\mathrm{d}\Phi}{\mathrm{d}R}\right)\right]+\mathcal{K}\left(\frac{\mathrm{d}W}{\mathrm{d}R}\right)^2=0, \tag{2.10}$$

where the dimensionless vdW traction reads:

$$Q(W)=\frac{1}{6}\left[\frac{1}{(W+1)^3}-\frac{1}{(W+1)^9}\right]. \tag{2.11}$$

Also, a Föppl–von Kármán number

$$\mathcal{K}=Et\sigma^2/2B \tag{2.12}$$

is defined by comparing the stretching strain energy ($\sim Et\varepsilon^2\sim Et(\sigma/\ell_{\rm vdW})^4$) with the bending strain energy ($\sim B\kappa^2\sim B\sigma^2/\ell_{\rm vdW}^4$), where ε is the characteristic in-plane strain and κ is the typical film curvature. Physically, as $\mathcal{K}$ increases, the energetic penalty for stretching becomes larger compared with that for bending. It is worth noting that, for regular films where $B=Et^3/12\left(1-\nu^2\right)$, $\mathcal{K}$ can be simplified as $6(1-\nu^2)(\sigma/t)^2$. For few-layer 2D materials, however, the value of $\mathcal{K}$ simplified this way may be somewhat underestimated due to interlayer slips [47,48]. Lastly, the dimensionless boundary conditions are given by:

$$W(\eta)=\delta,\quad W'(\eta)=0,\quad \Phi''(\eta)-\nu\frac{\Phi'(\eta)}{\eta}=(1-\nu)\tau,\quad \Phi(\eta)=0,$$
$$W(R)\to 0,\quad W'(R)\to 0,\quad \Phi(R)\to\frac{\tau R^2}{2}\quad \text{as}\quad R\to\infty. \tag{2.13}$$

In the numerical calculations, the "infinity" is placed at least at $R=1000$ to ensure the validity of those far-field boundary conditions.

It is then clear that the problem is characterized by four key dimensionless parameters. The first is the lifting/peeling height δ, which measures the vertical displacement of the loading region. The second is the loading radius η, which quantifies the size of the loading region relative to the characteristic bending length; when $\eta\ll 1$, the applied load can be approximated as a point force [49]. The third is the pre-tension τ, and the fourth is the Föppl–von Kármán number $\mathcal{K}$, which characterizes the relative importance of stretching and bending, with larger values corresponding to smaller resistance to bending deformation.

For experiments on graphite nanoflakes with thicknesses of 1–100 nm [19], representative values are $\sigma=$ 1–10 nm and $\Gamma\sim 0.1$ J/m^2. Over this thickness range, the bending stiffness increases dramatically, from approximately 1 to 10^8 eV [47,50,51]. These values give $\ell_{\rm vdW}\approx$ 0.6–300 nm, while $\tau\sim 1$ corresponds to a pre-tension of $\gamma\approx$ 1–10^2 N/m. Since experimentally used indenters or loading disks typically have radii from hundreds of nanometers to micrometers [19,40], and residual strains usually remain below 0.1% [52,53], regimes with excessively large pre-tension or very small loading radii are of limited experimental relevance. Accordingly, the present analysis is restricted to the following nondimensional parameter ranges:

$$\eta\gtrsim 1,\ \tau\ll 1,\mathcal{K}\lesssim 100. \tag{2.14}$$

3. Critical peeling force

3.1. The snap-through mechanism

Fig. 2a presents the numerical force–displacement curves obtained by solving Eqs. (2.9) and (2.10) subject to boundary conditions (2.13), using the `bvp4c` solver in MATLAB. These curves are calculated by displacement-controlled loading with $\tau=0$, $\mathcal{K}=30$, $\nu=0.165$. Under force-controlled loading (which is consistent with our experimental setup), however, the S-shaped curve leads to a limit-point instability once the critical peak force $\mathcal{F}_{\rm max}$ is reached (point A), after which the system jumps directly to point B. This transition corresponds to the snap-through phenomenon observed in previous experiments. Fig. 2b shows the film profiles before and after snap-through. During this transition, both the interfacial adhesion state and the film's deformation morphology change substantially. Therefore, this behavior might be important for the design of thin film devices with tunable adhesion and reversible switching between distinct deformation states, as recently demonstrated in Ref. [54].

Given the specified form of the van der Waals interaction, a crude estimate of the peeling force can be easily obtained by only integrating the van der Waals traction over the loading region: $F_{\rm in}=\int_0^a 2\pi q(d)\,r\mathrm{d}r$, where $q(w)$ has been introduced in Eq. (2.2). Its dimensionless form is

$$\mathcal{F}_{\rm in}=\int_0^\eta 2\pi Q(\delta)\,R\mathrm{d}R=\frac{\pi\eta^2}{6}\left[\frac{1}{(\delta+1)^3}-\frac{1}{(\delta+1)^9}\right]. \tag{3.1}$$

Apparently, this estimate depends only on the size of the loading region and is independent of material parameters such as film thickness. However, as shown in Fig. 2a, it underestimates the critical force: the prediction from Eq. (3.1), represented by the black dashed curves, lies well below the numerical solutions and becomes accurate only when the loading radius is sufficiently large. Moreover, this estimate is inconsistent with the experimentally measured peak peeling forces shown in the inset of Fig. 1b, which exhibit a pronounced thickness dependence. These observations indicate that film deformation outside the loading region contributes significantly to the peeling force required for snap-through, particularly when the loading size is relatively small. This contribution must therefore be carefully accounted for.

3.2. Correction from outside the loading region

As shown in Fig. 2b, the film deflection remains shallow prior to the snap transition, and the van der Waals spacing is near its equilibrium separation over the entire interface. Thus, the early-stage behavior can be understood from a linearized description of both the film deformation and the van der Waals interaction. Specifically, the only governing equation becomes the linearized out-of-plane equilibrium equation:

$$\nabla_R^4 W-\tau\nabla_R^2 W+W=0. \tag{3.2}$$

Here, ∇_R^2 denotes the axisymmetric Laplacian with respect to R, defined in the same way as in Eq. (2.1). Solving Eq. (3.2) reveals a linear force–displacement response, depending on both τ and η [49]. For our regime of interest given in Eq. (2.14) (i.e., large η and small τ), the total peeling force scales as:

$$\mathcal{F}=\mathcal{F}_{\rm in}+\mathcal{F}_{\rm out}\sim\frac{\pi\eta^2}{6}\left[\frac{1}{(\delta+1)^3}-\frac{1}{(\delta+1)^9}\right]+\eta\delta. \tag{3.3}$$

More derivational details of $\mathcal{F}_{\rm out}$ are provided in Appendix. In addition, the critical peeling height for snap-through is expected to be on the order of 1. This can be seen more clearly in Eq. (2.2), where the vdW traction reaches its maximum at the critical peeling height $\delta_{\rm in}=3^{1/6}-1$. Evaluating the force at this critical height gives the corrected estimate

$$\mathcal{F}_{\rm max}\approx\underbrace{\frac{\pi\eta^2}{6}\left[\frac{1}{\left(\delta_{\rm in}+1\right)^3}-\frac{1}{\left(\delta_{\rm in}+1\right)^9}\right]}_{\mathcal{F}_{\rm in}}+\underbrace{\eta\delta_{\rm in}}_{\mathcal{F}_{\rm out}}. \tag{3.4}$$

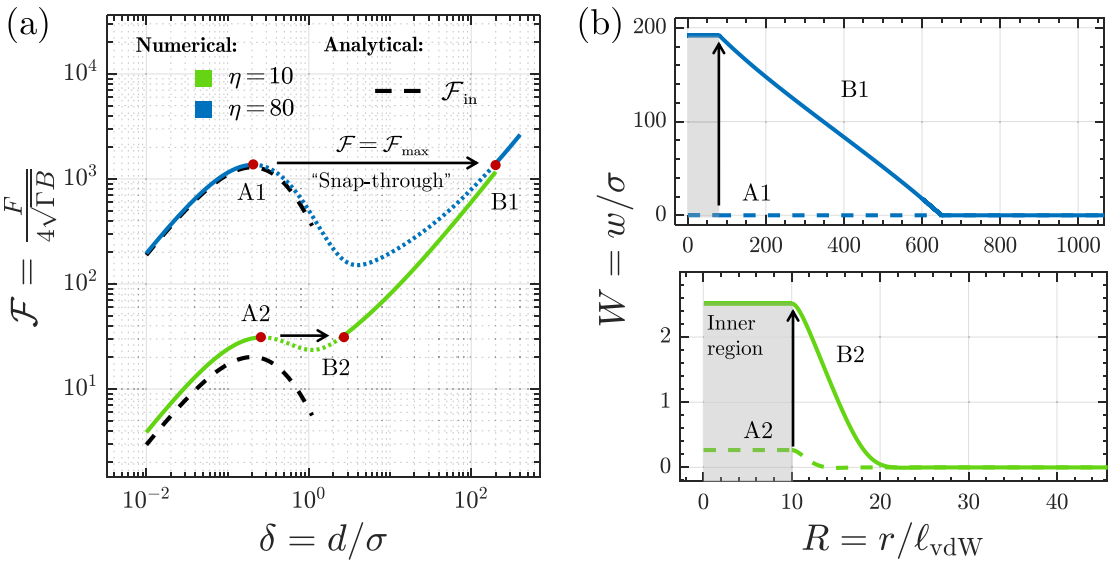


Fig. 2. (a) Numerical force–displacement curves for different dimensionless loading radii η. The colored curves show the full numerical solutions, while the black dashed curves are obtained by integrating the van der Waals traction within the loading region (Eq. (3.1)). Here, $\tau = 0$, $\mathcal{K} = 30$, $\nu = 0.165$. The red dots mark the states before and after snap through. (b) Film profiles before and after snap-through, corresponding to the marked points in panel (a). The shaded region denotes the inner region below the indenter, whose force contribution gives $\mathcal{F}_{\rm in}$ according to Eq. (3.1).

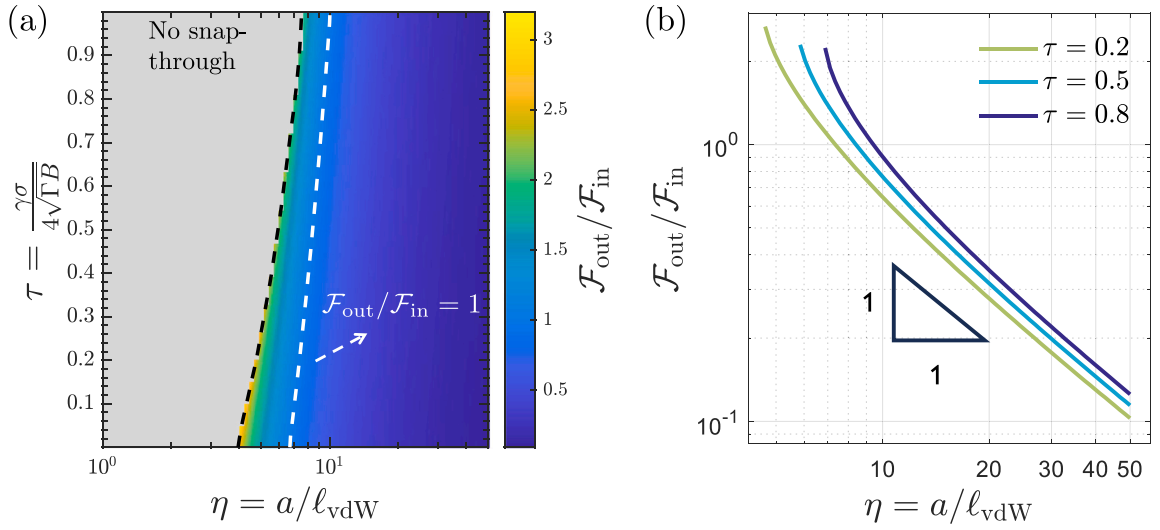


Fig. 3. Diagram in the $\eta - \tau$ space showing the magnitude of $\mathcal{F}_{\rm out}/\mathcal{F}_{\rm in}$ when snap-through occurs, calculated with $\mathcal{K} = 10$, $\nu = 0.165$. The gray region indicates the absence of snap-through, separated from the valid-data region by the black dashed curve. The white curve marks the boundary where $\mathcal{F}_{\rm out} = \mathcal{F}_{\rm in}$. (b) Variation of critical $\mathcal{F}_{\rm out}/\mathcal{F}_{\rm in}$ with η under different levels of pre-tension, with other parameters kept the same as in panel (a). The left end of the curve is truncated at the point where snap-through disappears.

Hereafter, the critical value of F_i or $\mathcal{F}_i$, with i = in or out, denotes the corresponding contribution to the critical peeling force at the onset of snap-through.

To further clarify when the contribution of $\mathcal{F}_{\rm out}$ must be taken into account, we construct an η–τ phase diagram of $\mathcal{F}_{\rm out}/\mathcal{F}_{\rm in}$ based on numerical calculations, as shown in Fig. 3a. The results are obtained for $\mathcal{K} = 10$, but the diagram shows no fundamental changes over the range $10 \lesssim \mathcal{K} \lesssim 100$. Interestingly, snap-through is suppressed below a critical loading radius, which increases slightly with pre-tension. Fig. 3b further quantifies how the relative contributions of $\mathcal{F}_{\rm out}$ and $\mathcal{F}_{\rm in}$ to the peak force vary with loading radius under different pre-tensions. The observed scaling $\mathcal{F}_{\rm out}/\mathcal{F}_{\rm in} \sim \eta^{-1}$ agrees with Eq. (3.4). As η increases, $\mathcal{F}_{\rm out}$ becomes progressively smaller relative to $\mathcal{F}_{\rm in}$, indicating that the peak peeling force is increasingly dominated by the direct contribution from vdW tractions in the loading region.

3.3. Thickness dependence of the snap-through force

After discussion on the outer deformation contribution $\mathcal{F}_{\rm out}$, we can now rationalize the thickness dependence of the critical peeling force. Since the critical peeling height is small, the bending stiffness of graphite flakes can be well approximated by $B \propto Et^3$ [47,48]. Accordingly, Eq. (3.4) gives a correction to the thickness dependence of the critical peeling force:

$$\mathcal{F}_{\rm out} = \frac{F_{\rm out}}{4\sqrt{\Gamma B}} \sim \frac{a}{\ell_{\rm vdW}} = \eta, \qquad F_{\rm out} \sim a\,\Gamma^{3/4} E^{1/4} t^{3/4} \sigma^{-1/2}. \tag{3.5}$$

In Fig. 4a, we plot the numerically calculated critical peeling force $F_{\rm out}$ as a function of the flake thickness by using experimental parameters $\sigma = 10$ nm, $\Gamma = 0.12$ N/m, $E = 0.96$ TPa, and $\nu = 0.165$. For relatively large loading radii, such as the two curves with $a \geqslant 1.5$ μm, a good

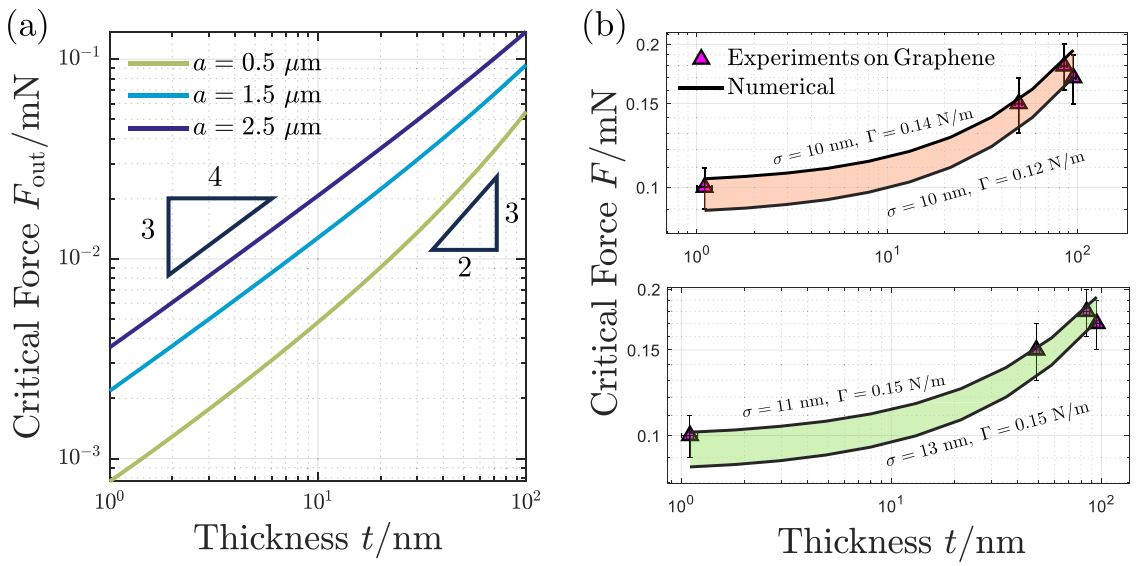


Fig. 4. (a) Numerically calculated dependence of critical F_{out} on the film thickness t. Here, $\sigma = 10$ nm, $\Gamma = 0.12$ N/m, $E = 0.96$ TPa, and $\nu = 0.165$ for graphene. (b) Extracted interfacial parameters obtained by fitting the numerical results to the experimental data. The remaining parameters are the same as those in panel (a).

agreement on scaling can be found between the numerical solutions and Eq. (3.5).

However, for smaller loading regions, such as $a = 0.5$ μm, noticeable deviations appear for relatively thick samples. This occurs because the dimensionless loading radius η already approaches order unity, so the large-η scaling in Eq. (3.5) is no longer applicable. In this regime, the system gradually crosses over toward the $\eta \ll 1$ limit, for which solving the linearized Eq. (3.2) gives $F_{out} \sim \Gamma^{1/2} E^{1/2} t^{3/2}$. In typical experiments where the sample thickness is varied [19], η spans a broad range, approximately from 10^0 to 10^2. Thus, the outer-region contribution F_{out} provides an essential correction to the peak peeling force, but its relative importance cannot be captured uniformly by a single limiting scaling law. Therefore, rather than relying on asymptotic scalings valid only in the limiting regimes of η, a more appropriate approach is to fit the experimentally measured F_{max} using the full numerical solutions of Eqs. (2.9)–(2.13).

In Fig. 4b, we keep E and ν fixed at the values used in Fig. 4a, while leaving Γ and σ as adjustable parameters. In the upper and lower panels, respectively, we adjust only Γ or σ to make the numerical curves of critical force versus flake thickness enclose the experimental data from above and below, which allows the corresponding parameter ranges to be determined. It can be seen that the numerical solutions capture well the thickness dependence of the peak force. Thus, the dependence of the peak force on the adhesion energy Γ and the equilibrium distance σ provides a route to infer key interfacial properties from this critical force measurement. In other words, if either Γ or σ is known, the numerical results can be fitted to the experimental data to determine the other parameter. This feature is of particular interest because the equilibrium distance is generally difficult to quantify using conventional experimental methods based on steady-state delamination [14].

4. Onset of wrinkling

Interestingly, snap-through in axisymmetric peeling tests is often accompanied by the emergence of wrinkles, as shown in Fig. 5a. This behavior can be naturally explained by the present model. Figs. 5b and 5c show the numerical distributions of the hoop stress, $\mathcal{N}_\theta$, in the film after snap-through, corresponding to point B in Fig. 2. For small pre-tension τ and large $\mathcal{K}$, pronounced hoop compression develops immediately after snap-through. The magnitude of this compression increases as τ decreases or $\mathcal{K}$ increases. The maximum hoop compressive stress also exhibits a weak non-monotonic dependence on the dimensionless loading radius η: it first increases and then decreases as η becomes larger. Overall, however, this variation with η remains relatively modest compared with the effects of pre-tension and film elasticity.

4.1. A near-threshold analysis

Observations above indicate that wrinkle formation driven by hoop compression must be considered after snap-through. We therefore examine the critical displacement for wrinkle onset, together with the corresponding wrinkling modes. The onset of wrinkling can be analyzed within the preceding axisymmetric framework by introducing small non-axisymmetric perturbations to the film deflection and the Airy stress functions. Specifically, we take

$$Z_{full}(R,\theta) = Z_0(R) + \varepsilon Z_1(R)\cos(n\theta) + \varepsilon^2 Z_2(R)\cos(n\theta) \tag{4.1}$$

and

$$\Phi_{full}(R,\theta) = \Phi_0(R) + \varepsilon \Phi_1(R)\cos(n\theta) + \varepsilon^2 \Phi_2(R)\cos(n\theta), \tag{4.2}$$

where the subscript 0 denotes the axisymmetric quantities obtained by solving Eqs. (2.9) and (2.10) without wrinkling, $\varepsilon \ll 1$ is a small perturbation parameter and n denotes the wrinkling wavenumber. Substituting the above expressions into the full (non-axisymmetric) Föppl–von Kármán equations yields:

$$\nabla^2\nabla^2 Z_{full}(R,\theta) - [Z_{full}(R,\theta), \Phi_{full}(R,\theta)] + \mathrm{vdW}(R,\theta) = 0 \tag{4.3}$$

and

$$\nabla^2\nabla^2 \Phi_{full}(R,\theta) + \mathcal{K}[Z_{full}(R,\theta), Z_{full}(R,\theta)] = 0, \tag{4.4}$$

where the vdW traction term is given as

$$\mathrm{vdW}(R,\theta) = \frac{1}{6}\left[\left(Z_{full}(R,\theta)+1\right)^{-3} - \left(Z_{full}(R,\theta)+1\right)^{-9}\right], \tag{4.5}$$

and operators now contain polar components:

$$\nabla^2 f = \frac{\partial^2 f}{\partial R^2} + \frac{1}{R}\frac{\partial f}{\partial R} + \frac{1}{R^2}\frac{\partial^2 f}{\partial \theta^2}$$

$$[f,t] = \frac{\partial^2 f}{\partial R^2}\left(\frac{1}{R}\frac{\partial t}{\partial R} + \frac{1}{R^2}\frac{\partial^2 t}{\partial \theta^2}\right) + \frac{\partial^2 t}{\partial R^2}\left(\frac{1}{R}\frac{\partial f}{\partial R} + \frac{1}{R^2}\frac{\partial^2 f}{\partial \theta^2}\right)$$

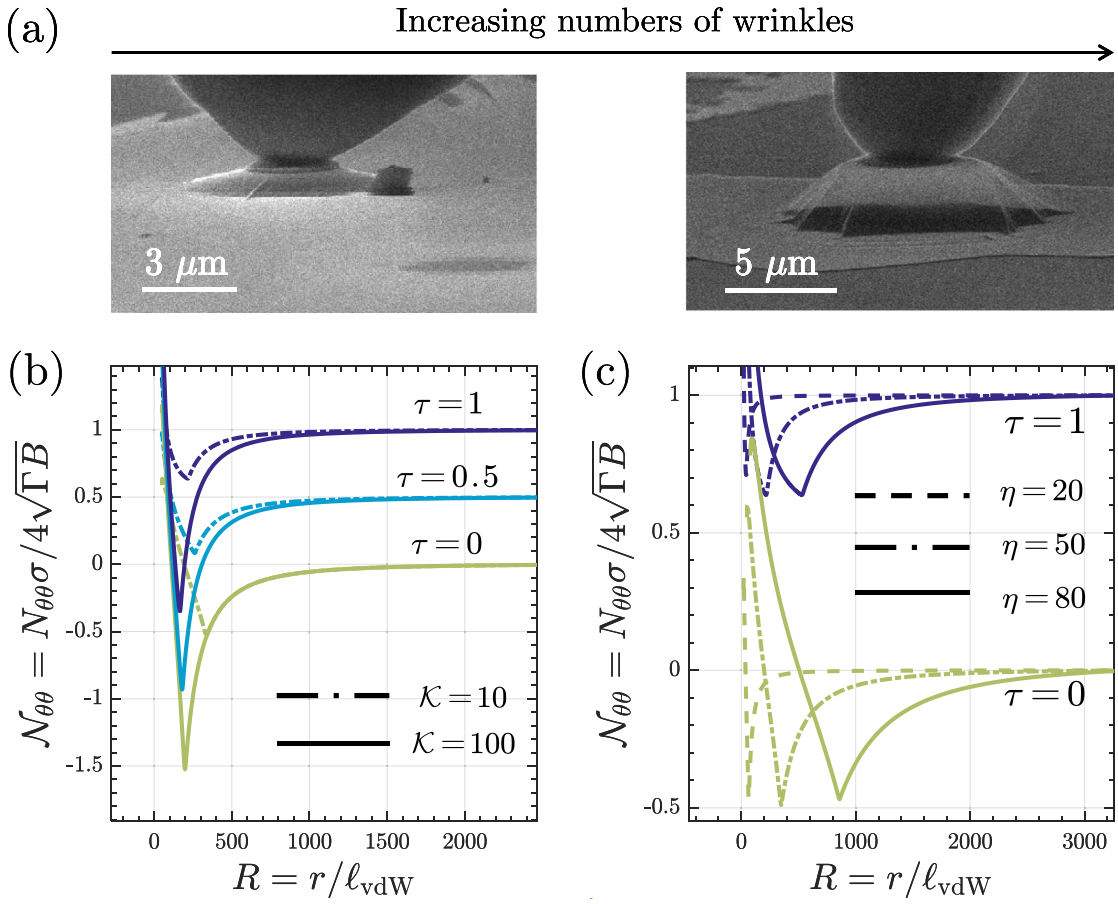


Fig. 5. (a) SEM images from axisymmetric peeling experiments on ∼10-nm-thick (left, relatively small η) and ∼1-nm-thick (right, relatively large η) graphite, showing increased wrinkle numbers. (b,c) Hoop-stress distributions corresponding to the post-snap-through state (point B in Fig. 2). Results are shown for (b) different $\mathcal{K}$ and τ with $\eta = 50$, $\nu = 0.165$, and (c) different η and τ with $\mathcal{K} = 10$, $\nu = 0.165$.

$$-2\frac{\partial}{\partial R}\left(\frac{1}{R}\frac{\partial f}{\partial \theta}\right)\frac{\partial}{\partial R}\left(\frac{1}{R}\frac{\partial t}{\partial \theta}\right).$$

Collecting terms according to the order of ε, the leading-order equations recover the axisymmetric Föppl–von Kármán Eqs. (2.9) and (2.10), while the first-order perturbation equations, corresponding to terms of order ε, take the following form:

$$\frac{\left[3-(1+Z_0)^6\right]Z_1}{2(1+Z_0)^{10}} + Z_1'''' + \frac{2}{R}Z_1''' - \frac{1+2n^2}{R^2}Z_1'' + \frac{1+2n^2}{R^3}Z_1' + \frac{n^2(n^2-4)}{R^4}Z_1 - \frac{1}{R^2}\left[\left(RZ_1' - n^2Z_1\right)\Phi_0'' + RZ_0'\Phi_1'' + \left(R\Phi_1' - n^2\Phi_1\right)Z_0'' + R\Phi_0'Z_1''\right] = 0, \tag{4.6}$$

and

$$\Phi_1'''' + \frac{2}{R}\Phi_1''' - \frac{1+2n^2}{R^2}\Phi_1'' + \frac{1+2n^2}{R^3}\Phi_1' + \frac{n^2(n^2-4)}{R^4}\Phi_1 + \frac{2\mathcal{K}}{R}Z_0'Z_1'' + \frac{2\mathcal{K}}{R}Z_1'Z_0'' - \frac{2\mathcal{K}n^2}{R^2}Z_1Z_0'' = 0. \tag{4.7}$$

Here, $()'$ denote differentiation with respect to R. The functions Z_n and Φ_n ($n = 0, 1, 2, \ldots$) depend only on R and have been written in abbreviated form. Also, since the governing equations must hold for arbitrary R and θ, the trigonometric factors have been omitted from the above equations.

With ε taken to be a small parameter, we assume that the boundary conditions of the system are fully satisfied by the leading-order solution $Z_0(R)$ and $\Phi_0(R)$. The first-order perturbation terms $Z_1(R)$ and $\Phi_1(R)$ can then be realized with homogeneous boundary conditions:

$$Z_1(\eta) = Z_1'(\eta) = 0, \qquad Z_1(\infty) = Z_1'(\infty) = 0 \tag{4.8}$$

and

$$\Phi_1(\eta) = 0, \qquad n\Phi_1''(\eta) - \nu\Phi_1'(\eta) = 0, \qquad \Phi_1'(\infty) = \Phi_1''(\infty) = 0. \tag{4.9}$$

Fortunately, we do not need to explicitly solve for the first-order terms. Instead, as long as the first-order equations, Eqs. (4.6) and (4.7), have nontrivial solutions, the axisymmetric configuration loses stability to a wrinkled state [43]. Accordingly, Eqs. (4.6) and (4.7), together with corresponding boundary conditions (4.8) and (4.9), are discretized with finite difference. A nontrivial solution exists when the determinant of the coefficient matrix is zero. The detailed implementation is as follows: For each integer wavenumber n, we identify the critical displacement δ_n at which the coefficient determinant first vanishes. The minimum value among all δ_n (we find that due to monotonicity, there exists one unique global minimum value) then determines the critical pulling displacement δ_c for wrinkle onset, while the corresponding value of n gives the number of wrinkles at the onset of this instability. The results when $\tau = 0$ are shown in Fig. 6. To reduce computational cost, the analysis is initiated from the displacement δ_{neg} at which negative hoop stress first appears. It is worth noting that, $\delta_c - \delta_{\mathrm{neg}}$ provides a more intrinsic measure of the film's resistance to compression-induced wrinkling than δ_c itself. This is because δ_{neg} is determined only by the axisymmetric deformation required to generate hoop compression, whereas $\delta_c - \delta_{\mathrm{neg}}$ measures the additional loading needed for this compression to overcome bending stabilization and trigger wrinkling.

4.2. Wrinkle criteria and number

In this section, we understand the dependence of the relative compression $\delta_c - \delta_{\mathrm{neg}}$ on $\mathcal{K}$ in Fig. 6 with a scaling analysis. The general

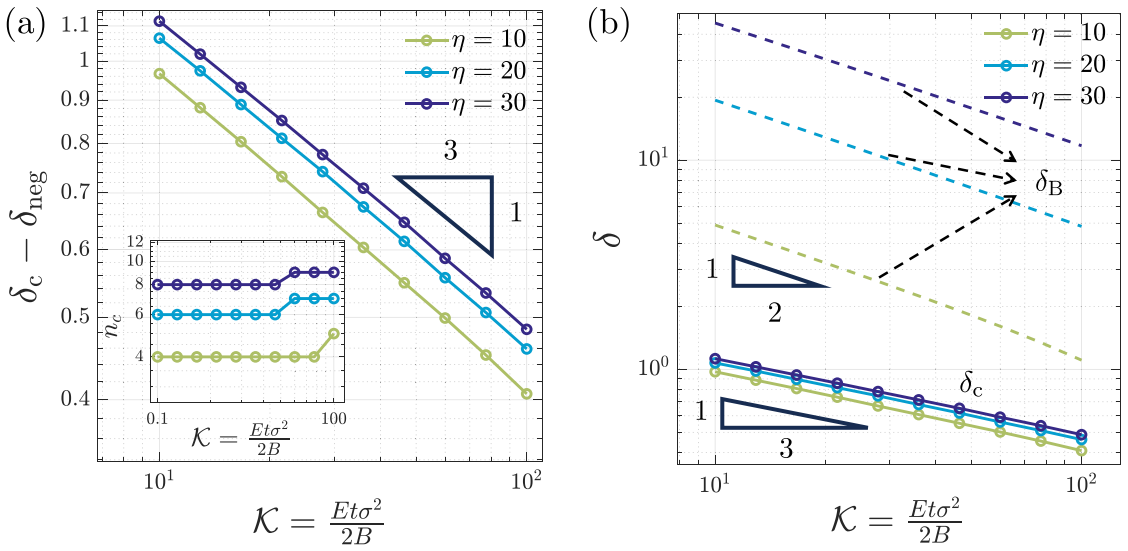


Fig. 6. (a) $\delta_c - \delta_{neg}$ as a function of $\mathcal{K}$ for different loading radii η. The inset shows the corresponding wrinkle number n as a function of $\mathcal{K}$. (b) Critical wrinkling displacement δ_c (solid lines) and post-snap-through lifting height δ_B (dashed lines, denoting the displacement corresponding to the post-snap-through point in Fig. 2a) as functions of $\mathcal{K}$ for different loading radii η. Both (a) and (b) are obtained when $\tau = 0, \nu = 0.165$.

strategy is inspired by [55]. Differently, in the zero-pretension regime considered here, the in-plane stress in the film is no longer set by the applied pre-tension, but is instead dominated by nonlinear stretching. This difference calls for a modified scaling analysis.

According to Eq. (2.10), the magnitude of the in-plane stress can be estimated as (for clarity, the following discussion is conducted in the nondimensional framework):

$$\mathcal{N}_R \sim \mathcal{N}_\theta \sim \mathcal{K}. \tag{4.10}$$

We denote the radial position of the minimum hoop stress by R_*, and the characteristic curvature of the local stress valley by $1/L_*$. As shown in Figs. 5b and 5c, R_* remains of the same order of magnitude for different values of $\mathcal{K}$, and the local stress profiles around minimum are approximately self-similar. In contrast, variations in η leads to much more significant changes in the hoop-stress distribution. A larger η leads to a broader hoop-compression region, with the location of maximum compression shifting markedly outward. We therefore assume in the following that

$$R_* \sim R_*(\eta), \quad L_* \sim L_*(\eta). \tag{4.11}$$

When η is fixed, the distribution of $\mathcal{N}_\theta$ evolves with the lifting height and can thus be expressed as a function of R and δ. To understand the distribution of $\mathcal{N}_\theta(R, \delta)$ at the onset of hoop compression, we denote by $R_* = R_*^0$ where the minimum hoop stress first reaches zero. Namely, $\mathcal{N}_\theta(R_*^0, \delta_{neg}) = 0$ where $L_* = L_*^0$. In this way, the circumferential stress may be expanded locally around the critical point (R_*^0, δ_{neg}):

$$\begin{aligned}\mathcal{N}_\theta(R,\delta) = \mathcal{N}_\theta(R_*^0,\delta_{neg}) &+ \left.\frac{\partial \mathcal{N}_\theta}{\partial R}\right|_* (R - R_*^0) + \left.\frac{\partial \mathcal{N}_\theta}{\partial \delta}\right|_* (\delta - \delta_{neg}) \\ &+ \frac{1}{2}\left.\frac{\partial^2 \mathcal{N}_\theta}{\partial R^2}\right|_* (R - R_*^0)^2 + \left.\frac{\partial^2 \mathcal{N}_\theta}{\partial R \partial \delta}\right|_* (R - R_*^0)(\delta - \delta_{neg}) \\ &+ \frac{1}{2}\left.\frac{\partial^2 \mathcal{N}_\theta}{\partial \delta^2}\right|_* (\delta - \delta_{neg})^2 + \cdots,\end{aligned} \tag{4.12}$$

where the subscript $*$ denotes evaluation at (R_*^0, δ_{neg}). Since $R = R_*^0$ is a zero-valued local minimum of $\mathcal{N}_\theta$, the first, second, and fourth terms in the above equation all vanish, so Eq. (4.12) can be further simplified as:

$$\mathcal{N}_\theta(R,\delta) \approx \left.\frac{\partial \mathcal{N}_\theta}{\partial \delta}\right|_* (\delta - \delta_{neg}) + \frac{1}{2}\left.\frac{\partial^2 \mathcal{N}_\theta}{\partial R^2}\right|_* (R - R_*^0)^2. \tag{4.13}$$

The validity of neglecting other second-derivative terms will be further justified later. Furthermore, according to Eqs. (4.10) and (4.11), at the onset of wrinkling, the local stress distribution near R_* reads:

$$(-\mathcal{N}_\theta)_{max} \sim \mathcal{K}\Delta\delta, \qquad \mathcal{N}_\theta(R) \sim \mathcal{K}\Delta\delta + \mathcal{K}\left(\frac{R - R_*^0}{L_*^0}\right)^2, \tag{4.14}$$

where Eq. (4.11) is used to replace the derivatives, $\Delta\delta = \delta_c - \delta_{neg}$, and the prefactors have been omitted since they do not affect the subsequent analysis. Here, since the maximum compressive stress $(-\mathcal{N}_\theta)_{max}$ still occurs near R_*^0 acoording to Eq. (4.11), only the expansion terms associated with $\Delta\delta$ are included. From $\mathcal{N}_\theta = 0$, we solve for the compressed region width $L_w = R|_{\mathcal{N}_\theta=0} - R_*^0 \sim L_*^0 \Delta\delta^{1/2}$, which gives our first estimate of the stress state.

In addition, the dominant normal force contributions at wrinkling onset are balanced according to Eq. (4.3), including the bending term ($\sim n^4 W/(R_*^0)^4$), the radial stretching contribution ($\sim \mathcal{K}W/L_w^2$), and the circumferential contribution ($\sim \mathcal{K}\Delta\delta\, n^2\, W/(R_*^0)^2$). The three balances above yield the following result:

$$L_w \sim (L_*^0)^{2/3}\mathcal{K}^{-1/6}, \quad n \sim R_*^0 (L_*^0)^{-1/3}\mathcal{K}^{1/3}, \quad \Delta\delta \sim (L_*^0)^{-2/3}\mathcal{K}^{-1/3}. \tag{4.15}$$

Since R_*^0, L_*^0 are independent of $\mathcal{K}$, this scaling law of $\Delta\delta \sim \mathcal{K}^{-1/3}$ is well validated by the numerical results, as shown in Fig. 6a. Meanwhile, Eq. (4.15) also proves that the second-derivative terms neglected in Eq. (4.13) are asymptotically small when $\mathcal{K} \gg 1$, thereby confirming the self-consistency of our theory.

The scaling with respect to n is not clearly observed in the present results. This may be because the range of $\mathcal{K}$ considered here is not sufficiently large, while the corresponding values of n remain relatively small. Nonetheless, the increased wrinkle number in relatively thin samples (hence of relatively large $\mathcal{K}$) agrees with the observation in Fig. 6a qualitatively. However, excessively large values of $\mathcal{K}$ fall beyond the scope of the present study. At the same time, both the "over-lifting height" $\Delta\delta = \delta_c - \delta_{neg}$ for wrinkling and the critical wrinkle number n increase slightly with the dimensionless loading radius η at fixed $\mathcal{K}$, as shown in Fig. 6.

4.3. Axisymmetric limits and wrinkle formation

If wrinkling is not considered, the lifting height after axisymmetric snap-through is denoted by δ_B. Therefore, $\delta_c < \delta_B$ indicates that

wrinkling has already occurred in the film after snap-through. Meanwhile, because $\delta_c \ll \delta_B$, the wrinkles observed in our experiments, for example in Fig. 5, have already undergone post-buckling evolution and may therefore include sharp ridges or folds. Following the work of [56], bending effects are subdominant for $\delta \gg 1$, so that the force–displacement relation may be estimated by a membrane-like analysis:

$$F \sim (Et\Gamma)^{1/2} d \text{ or } \mathcal{F} \sim \mathcal{K}^{1/2}\delta. \tag{4.16}$$

The linearized analysis in Section 3 indicates that the peak force is governed primarily by the van der Waals traction and film bending, with a minor contribution from nonlinear stretching. Therefore, $\mathcal{K}$, which enters only through the compatibility equation Eq. (2.10), has little influence on the peak force. We may therefore infer from Eq. (4.16) that: $\delta_B \sim \mathcal{K}^{-1/2}$, which is validated by the dashed lines in Fig. 6b. Meanwhile, we find that δ_c still follows the $\mathcal{K}^{-1/3}$ scaling law for $\tau = 0$. This is because at small pre-tension, δ_{neg} remains very small and then has a weak influence on the scaling of $\delta_c - \delta_{neg}$. As shown in Fig. 6b, we find $\delta_c \ll \delta_B$ throughout the range of $10 \leqslant \mathcal{K} \leqslant 100$, with the separation between these two (dashed and solid curves) becoming particularly pronounced at larger η. Although δ_B decreases faster than δ_c with increasing $\mathcal{K}$, which suggest that $\delta_B < \delta_c$ could occur in the limit of very small η and large $\mathcal{K}$ (this extreme regime may even allow $\delta_c < \delta_A$ mathematically), we want to emphasize that this regime is unlikely to be accessible experimentally. Meanwhile, under these conditions, as shown in Fig. 3a, snapthrough may no longer exist. Therefore, under typical experimental conditions [19], wrinkling is expected to occur right after snap-through, which provides a natural explanation for previous experimental observations [19,37,57].

5. Conclusions

In this work, we have investigated the axisymmetric peeling of thin elastic films from a rigid substrate under cylindrical loading, focusing on the onset of snap-through and the subsequent wrinkling instability. By incorporating a nonlinear van der Waals traction law into a Föppl–von Kármán plate model, we developed a unified framework for describing the early-stage peeling process before the formation of a steady blister. The analysis shows that the critical peeling force cannot be determined solely from the van der Waals traction acting within the loading region. Instead, deformation outside the loading region provides an important additional contribution, especially when the dimensionless loading radius η is not sufficiently large. This outer-region correction explains the experimentally observed thickness dependence of the peak peeling force and provides a practical route for extracting interfacial parameters, such as the adhesion energy Γ and equilibrium separation σ, from critical peeling force measurements.

We further examined the onset of wrinkling after snap-through by introducing small non-axisymmetric perturbations to the axisymmetric solution. The post-snap-through state develops hoop compression, which can destabilize the axisymmetric configuration and trigger wrinkle formation. The resulting near-threshold eigenvalue analysis determines both the critical wrinkling displacement and the corresponding wrinkle number. In the absence of pre-tension, the numerical results are well captured by the scaling law $\delta_c - \delta_{neg} \sim \mathcal{K}^{-1/3}$, indicating that the resistance to compression-induced wrinkling is primarily governed by the film elasticity. Comparison between the wrinkling threshold and the post-snap-through lifting height further suggests that, under typical experimental conditions, wrinkling occurs almost immediately after snap-through. Overall, these results clarify how interfacial adhesion, film elasticity, and loading geometry jointly govern instability-mediated peeling and provide theoretical guidance for interpreting axisymmetric peeling experiments and designing thin-film or 2D material systems with tunable adhesion and switchable deformation states.

CRediT authorship contribution statement

Erteng Chen: Writing – original draft, Validation, Software, Methodology, Investigation, Formal analysis, Data curation. **Zheng Fang:** Methodology, Data curation. **Xianlong Wei:** Writing – review & editing, Supervision, Data curation, Conceptualization. **Zhaohe Dai:** Writing – review & editing, Supervision, Formal analysis, Conceptualization.

Declaration of competing interest

The authors declare that they have no known competing financial interests or personal relationships that could have appeared to influence the work reported in this paper.

Acknowledgments

This work was supported by the National Natural Science Foundation of China (Grant Nos. 12372103, 12432003, and 12625205).

Appendix. Outer-region contribution to the peeling force

Here we briefly derive the outer-region force contribution used in Eq. (3.3). Outside the contact region, $R > \eta$, the deformation is governed by the linearized plate-on-foundation equation:

$$\nabla_R^4 W - \tau \nabla_R^2 W + W = 0. \tag{A.1}$$

The boundary conditions at the periphery of the indenter are

$$W(\eta) = \delta, \qquad W'(\eta) = 0,$$

while the far-field conditions are

$$W(R) \to 0, \qquad W'(R) \to 0, \qquad R \to \infty.$$

Eq. (A.1) can be factorized as

$$(\nabla_R^2 - \lambda_+)(\nabla_R^2 - \lambda_-)W = 0,$$

where

$$\lambda_\pm = \frac{\tau \pm \sqrt{\tau^2 - 4}}{2}.$$

The axisymmetric solution is therefore

$$W(R) = C_1 K_0(\lambda_+^{1/2} R) + C_2 K_0(\lambda_-^{1/2} R),$$

where K_n denotes the modified Bessel function of the second kind. Defining $K_{0\pm} = K_0(\lambda_\pm^{1/2}\eta)$, $K_{1\pm} = K_1(\lambda_\pm^{1/2}\eta)$, the two constants are obtained as

$$C_1 = \frac{K_{1-}\lambda_-^{1/2}\delta}{K_{0+}K_{1-}\lambda_-^{1/2} - K_{0-}K_{1+}\lambda_+^{1/2}},$$

and

$$C_2 = \frac{K_{1+}\lambda_+^{1/2}\delta}{K_{0-}K_{1+}\lambda_+^{1/2} - K_{0+}K_{1-}\lambda_-^{1/2}}.$$

The outer-region force is then obtained by integrating the restoring traction from the foundation outside the contact region,

$$\mathcal{F}_{out} = 2\pi \int_\eta^\infty W(R) R \, \mathrm{d}R.$$

Therefore, we obtain a linear force–displacement relation,

$$\mathcal{F}_{out} = K_{out}\delta,$$

with the outer indentation stiffness

$$K_{out} = 2\pi\eta \left(C_1 \lambda_+^{-1/2} K_{1+} + C_2 \lambda_-^{-1/2} K_{1-} \right) / \delta.$$

This expression is the complete linear stiffness of the outer region. Through an asymptotic analysis of the Bessel functions, the stiffness in the parameter regime considered in this work can be obtained as:

$$K_{\text{out}} \sim 2\sqrt{2}\pi\eta \qquad \text{for} \qquad \eta \gg 1,\ \tau \ll 1.$$

Thus, for the scaling estimate used in the main text,

$$\mathcal{F}_{\text{out}} = K_{\text{out}}\delta \sim \eta\delta.$$

In addition, we have

$$K_{\text{out}} \sim 8 \qquad \text{for} \qquad \eta \ll 1,\ \tau \ll 1,$$

which leads to the secondary scaling in Section 3.3. More details and physical interpretation can be found in [49].

Data availability

Data will be made available on request.

References

[1] A. Berman, I. Lee, R. Raman, Compliant in vitro bioelectronics: Biohybrid device design strategies with materials and structures, Extrem. Mech. Lett. (2026) 102487.

[2] D. Akinwande, N. Petrone, J. Hone, Two-dimensional flexible nanoelectronics, Nat. Commun. 5 (1) (2014) 5678.

[3] D. Akinwande, C.J. Brennan, J.S. Bunch, P. Egberts, J.R. Felts, H. Gao, R. Huang, J.-S. Kim, T. Li, Y. Li, et al., A review on mechanics and mechanical properties of 2D materials–graphene and beyond, Extrem. Mech. Lett. 13 (2017) 42–77.

[4] Z. Dai, L. Liu, Z. Zhang, Strain engineering of 2D materials: issues and opportunities at the interface, Adv. Mater. 31 (45) (2019) 1805417.

[5] W. Zheng, Z. Gao, C. Yu, J. Yin, Z. Dai, Revealing surface tension in elastic membranes via indentation, Extrem. Mech. Lett. (2026) 102455.

[6] Y. Chen, Y. Lin, C. Feng, K. Kang, H. Liu, P. Ying, Y. Yang, Y. Liu, Unified theoretical framework for thermal expansion engineering in multilayer 2D materials, Extrem. Mech. Lett. (2026) 102474.

[7] Z. Dong, J. Bai, D. Yin, K. Yu, S. Yan, Z. Sheng, Z. Jia, Chebyshev physics-informed Kolmogorov-Arnold networks for diffusion-convection-reaction equation in soft material adhesion system, Extrem. Mech. Lett. (2025) 102436.

[8] L.B. Freund, S. Suresh, Thin Film Materials: Stress, Defect Formation and Surface Evolution, Cambridge University Press, 2004.

[9] C.W. Barney, Y.L. Zheng, Peeling a rigid sphere from a stretched rubber substrate, Extrem. Mech. Lett. (2025) 102381.

[10] J. Deng, C. Linghu, S. Zhang, Z. Ng, D. Low, H. Gao, K.J. Hsia, H. Lu, Peeling adhesion regime transition of elastic tapes, Extrem. Mech. Lett. (2025) 102414.

[11] X. Li, M. Sun, C. Shan, Q. Chen, X. Wei, Mechanical properties of 2D materials studied by in situ microscopy techniques, Adv. Mater. Interfaces 5 (5) (2018) 1701246.

[12] N. Iguiñiz, R. Frisenda, R. Bratschitsch, A. Castellanos-Gomez, Revisiting the buckling metrology method to determine the Young's modulus of 2D materials, Adv. Mater. 31 (10) (2019) 1807150.

[13] K.-T. Wan, Y.-W. Mai, Fracture mechanics of a shaft-loaded blister of thin flexible membrane on rigid substrate, Int. J. Fract. 74 (2) (1996) 181–197.

[14] Z. Dai, N. Lu, K.M. Liechti, R. Huang, Mechanics at the interfaces of 2D materials: Challenges and opportunities, Curr. Opin. Solid State Mater. Sci. 24 (4) (2020) 100837.

[15] J. Chopin, D. Vella, A. Boudaoud, The liquid blister test, Proc. R. Soc. A: Math. Phys. Eng. Sci. 464 (2099) (2008) 2887–2906.

[16] S.P. Koenig, N.G. Boddeti, M.L. Dunn, J.S. Bunch, Ultrastrong adhesion of graphene membranes, Nature Nanotechnology 6 (9) (2011) 543–546.

[17] N.G. Boddeti, S.P. Koenig, R. Long, J. Xiao, J.S. Bunch, M.L. Dunn, Mechanics of adhered, pressurized graphene blisters, J. Appl. Mech. 80 (4) (2013) 040909.

[18] Z. Dai, N. Lu, Poking and bulging of suspended thin sheets: Slippage, instabilities, and metrology, J. Mech. Phys. Solids 149 (2021) 104320.

[19] Z. Fang, Z. Dai, B. Wang, Z. Tian, C. Yu, Q. Chen, X. Wei, Pull-to-peel of two-dimensional materials for the simultaneous determination of elasticity and adhesion, Nano Lett. 23 (2) (2022) 742–749.

[20] C. Sun, J. Sun, J. Leng, Blister deformation and interlayer delamination in shaft-loaded bilayer films, Extrem. Mech. Lett. 83 (2026) 102458.

[21] K.-T. Wan, S. Guo, D.A. Dillard, A theoretical and numerical study of a thin clamped circular film under an external load in the presence of a tensile residual stress, Thin Solid Films 425 (1–2) (2003) 150–162.

[22] D. Vella, B. Davidovitch, Indentation metrology of clamped, ultra-thin elastic sheets, Soft Matter 13 (11) (2017) 2264–2278.

[23] J. Cao, Z. Dai, C. Yu, W. Wang, X. Wei, Y. Wei, Fracture mechanics of 2D crystal blisters with irregular geometry, Adv. Funct. Mater. 36 (1) (2026) e09438.

[24] C. Sun, H. Che, J. Sun, F. Jia, J. Leng, Shaft-loaded blister peeling test of hyperelastic membranes on the rigid substrate, Int. J. Solids Struct. (2025) 113720.

[25] X. Yang, L. Yu, R. Long, Contact mechanics of inflated circular membrane under large deformation: Analytical solutions, Int. J. Solids Struct. 233 (2021) 111222.

[26] W. Zheng, Z. Dai, Universal pull-off force for separating a rigid sphere from a membrane, J. Mech. Phys. Solids 201 (2025) 106163.

[27] W. Zeng, Z. Dai, Y. Wei, Adhesion of elastic membranes. Part I: a generalized tabor parameter, Proc. R. Soc. A Math. Phys. Eng. Sci. 482 (2330) (2026) 20250932.

[28] M.M. Talukder, E. Washburn, B. Behkam, S. Kale, Spreading, adhesion, and pull-off of turgor-pressurized enclosed membranes on curved substrates, Int. J. Solids Struct. (2026) 114060.

[29] A. Castellanos-Gomez, R. Roldán, E. Cappelluti, M. Buscema, F. Guinea, H.S. Van Der Zant, G.A. Steele, Local strain engineering in atomically thin MoS2, Nano Lett. 13 (11) (2013) 5361–5366.

[30] W. Dong, Z. Dai, L. Liu, Z. Zhang, Toward clean 2D materials and devices: recent progress in transfer and cleaning methods, Adv. Mater. 36 (22) (2024) 2303014.

[31] H. Long, Y. Liu, H. Yin, Y. Zhang, Q. Yang, Y. Wei, 90-Degree peeling of elastic thin films from elastic soft substrates: Theoretical solutions and experimental verification, J. Mech. Phys. Solids 193 (2024) 105855.

[32] H. Yin, Z. Peng, Y. Yao, S. Chen, H. Gao, A general solution to the maximum detachment force in thin film peeling, Int. J. Solids Struct. 242 (2022) 111546.

[33] Z. Peng, S. Chen, Effect of bending stiffness on the peeling behavior of an elastic thin film on a rigid substrate, Phys. Rev. E 91 (4) (2015) 042401.

[34] C. Yu, Z. Dai, Premature jump-to-contact with elastic surfaces, J. Mech. Phys. Solids 193 (2024) 105919.

[35] Z. Dai, Jump of an atomic force microscopy probe towards an elastic substrate in a liquid environment, J. Fluid Mech. 1013 (2025) A49.

[36] J. Zang, S. Ryu, N. Pugno, Q. Wang, Q. Tu, M.J. Buehler, X. Zhao, Multifunctionality and control of the crumpling and unfolding of large-area graphene, Nat. Mater. 12 (4) (2013) 321–325.

[37] Z. Dai, D.A. Sanchez, C.J. Brennan, N. Lu, Radial buckle delamination around 2D material tents, J. Mech. Phys. Solids 137 (2020) 103843.

[38] A. Juel, D. Pihler-Puzović, M. Heil, Instabilities in blistering, Annu. Rev. Fluid Mech. 50 (2018) 691–714.

[39] C. Linghu, H. Zhu, J. Zhu, C. Li, J. Song, Mechanics of magnet-controlled transfer printing, Extrem. Mech. Lett. 27 (2019) 76–82.

[40] C. Yu, W. Zeng, B. Wang, X. Cui, Z. Gao, J. Yin, L. Liu, X. Wei, Y. Wei, Z. Dai, Stiffer is stickier: Adhesion in elastic nanofilms, Nano Lett. 25 (5) (2024) 1876–1882.

[41] C. Yu, W. Zeng, Z. Kou, W. Wang, L. Wang, Q. Li, X. Liu, Z. Dai, Transparency of graphene to solid-solid van der Waals interactions, Phys. Rev. Lett. 135 (15) (2025) 156202.

[42] E.H. Mansfield, The Bending and Stretching of Plates, 1989.

[43] F. Box, D. Vella, R.W. Style, J.A. Neufeld, Indentation of a floating elastic sheet: geometry versus applied tension, Proc. Math. Phys. Eng. Sci. 473 (2206) (2017) 20170335.

[44] J.N. Israelachvili, Intermolecular and Surface Forces, Academic Press, 2011.

[45] Z. Liu, M. Amani, S. Najmaei, Q. Xu, X. Zou, W. Zhou, T. Yu, C. Qiu, A.G. Birdwell, F.J. Crowne, et al., Strain and structure heterogeneity in MoS2 atomic layers grown by chemical vapour deposition, Nat. Commun. 5 (1) (2014) 5246.

[46] S.-W. Wang, H. Medina, K.-B. Hong, C.-C. Wu, Y. Qu, A. Manikandan, T.-Y. Su, P.-T. Lee, Z.-Q. Huang, Z. Wang, et al., Thermally strained band gap engineering of transition-metal dichalcogenide bilayers with enhanced light–matter interaction toward excellent photodetectors, ACS Nano 11 (9) (2017) 8768–8776.

[47] G. Wang, Z. Dai, J. Xiao, S. Feng, C. Weng, L. Liu, Z. Xu, R. Huang, Z. Zhang, Bending of multilayer van der Waals materials, Phys. Rev. Lett. 123 (11) (2019) 116101.

[48] E. Han, J. Yu, E. Annevelink, J. Son, D.A. Kang, K. Watanabe, T. Taniguchi, E. Ertekin, P.Y. Huang, A.M. van der Zande, Ultrasoft slip-mediated bending in few-layer graphene, Nat. Mater. 19 (3) (2020) 305–309.

[49] E. Chen, Z. Dai, Elastic sheets on Winkler foundations: Indentation stiffness and nonlinearities, Int. J. Solids Struct. 315 (2025) 113346.

[50] K.N. Kudin, G.E. Scuseria, B.I. Yakobson, C 2 F, BN, and C nanoshell elasticity from ab initio computations, Phys. Rev. B 64 (23) (2001) 235406.

[51] Q. Lu, M. Arroyo, R. Huang, Elastic bending modulus of monolayer graphene, J. Phys. D: Appl. Phys. 42 (10) (2009) 102002.

[52] S. Luo, C.P. Cullen, G. Guo, J. Zhong, G.S. Duesberg, Investigation of growth-induced strain in monolayer MoS2 grown by chemical vapor deposition, Appl. Surf. Sci. 508 (2020) 145126.

[53] S. Kataria, S. Wagner, T. Cusati, A. Fortunelli, G. Iannaccone, H. Pandey, G. Fiori, M.C. Lemme, Growth-induced strain in chemical vapor deposited monolayer MoS2: experimental and theoretical investigation, Adv. Mater. Interfaces 4 (17) (2017) 1700031.

[54] N. Ronceray, M. Spina, V.H.Y. Chou, C.T. Lim, A.K. Geim, S. Garaj, Elastocapillarity-driven 2D nano-switches enable zeptoliter-scale liquid encapsulation, Nat. Commun. 15 (1) (2024) 185.
[55] D. Vella, B. Davidovitch, Regimes of wrinkling in an indented floating elastic sheet, Phys. Rev. E 98 (1) (2018) 013003.
[56] E. Chen, Z. Dai, Axisymmetric peeling of thin elastic films: A perturbation solution, J. Appl. Mech. 90 (10) (2023) 101011.
[57] Z. Zong, C.-L. Chen, M.R. Dokmeci, K.-t. Wan, Direct measurement of graphene adhesion on silicon surface by intercalation of nanoparticles, J. Appl. Phys. 107 (2) (2010).